doi: 10.1093/pasj/xxx000

arXiv:2105.05421v1 [astro-ph.GA] 12 May 2021

Three-dimensional dust geometry of the LMC H I ridge region as revealed by the IRSF/SIRIUS survey

Takuya FURUTA[1]*, Hidehiro KANEDA[1], Takuma KOKUSHO[1], Yasushi NAKAJIMA[2], Yasuo FUKUI,[1] and Kisetsu TSUGE,[1]

[1]Graduate School of Science, Nagoya University, Furo-cho, Chikusa-ku, Nagoya, Aichi 464-8602, Japan

[2]National Astronomical Observatory of Japan, 2-21-1 Osawa, Mitaka, Tokyo 181-8588, Japan

*E-mail: t.furuta@u.phys.nagoya-u.ac.jp

Received ; Accepted 2021 May 10

Abstract

We present a new method to evaluate the dust extinction (A_V) along the line of sight using the InfraRed Survey Facility (IRSF) near-infrared (NIR) data of the Large Magellanic Cloud (LMC) H I ridge region. In our method, we estimate an A_V value for each star from the NIR color excess and sort them from bluer to redder in each line of sight. Using the percentile values of the sorted A_V, we newly construct the three-dimensional A_V map. We compare the resultant A_V map with the total hydrogen column density N(H) traced by velocity-resolved H I and CO observations. In the LMC H I ridge region, Fukui et al. (2017, PASJ, 69, L5) find two velocity components and an intermediate velocity one bridging them. Comparing our three-dimensional A_V maps with N(H) maps at the different velocities, we find that the dust geometry is consistent with the scenario of the on-going gas collision between the two velocities as suggested in the previous study. In addition, we find difference by a factor of 2 in A_V/N(H) between the two velocity components, which suggests that inflow gas from the Small Magellanic Clouds (SMC) is mixed in this region. As a whole, our results support the triggered star formation in 30 Doradus due to the large-scale gas collision caused by tidal interaction between the LMC and the SMC.

Key words: dust, extinction — Magellanic Clouds — ISM: structure — infrared: ISM

1 Introduction

The Large Magellanic Cloud (LMC) represents an ideal laboratory for studying the interstellar medium (ISM) among external galaxies. Because of its proximity ($\simeq$ 50 kpc; Pietrzyński et al. 2019) and its nearly face-on orientation ($i \sim 35°$; van der Marel & Cioni 2001), we can perform spatially well-resolved studies of the ISM in almost two dimensions. In addition, the LMC is a suitable site for studying massive star formation in low metallicity environments ($Z \sim 0.5$ Z$_\odot$; Westerlund 1997). In the LMC H I ridge region, several massive star formations have been reported in 30 Doradus (30 Dor; e.g., Fukui et al. 2017; Indebetouw et al. 2020) and N159 (e.g., Fukui et al. 2019; Tokuda et al. 2019). In particular, 30 Dor is the most extreme starburst in the Local Universe. 30 Dor harbors about 400 O-type/Wolf-Rayet stars, primarily powered by the central super star cluster R136 (Doran et al. 2013). R136 has the mass of 5.0×10^4 M$_\odot$, 10 times larger than that of a super star cluster in our Galaxy and hosts the most massive stars heavier than 200 M$_\odot$ (Crowther et al. 2010; Crowther et al. 2016; Schneider et al. 2018).

© 2018. Astronomical Society of Japan.

A recent study suggests that massive O- and B-type stars in R136 were formed by collision of H I clouds (Fukui et al. 2017). In their study, two velocity components of H I clouds and an intermediate velocity one bridging them are identified, from which they suggest that massive star formation in 30 Dor has been triggered by collision between these two velocity components. In addition, they compare the dust optical depth at 353 GHz, τ_{353}, with the H I intensity W(H I), and find that τ_{353}/W(H I) in the H I ridge region is lower than that outside the H I ridge region. They suggest that the lower τ_{353}/W(H I) ratio is caused by the contamination of inflow gas from the Small Magellanic Cloud (SMC), which is known to have even lower metallicity gas than the LMC, based on the result of the numerical simulation (Bekki & Chiba 2007a; Bekki & Chiba 2007b; Yozin & Bekki 2014). Hence the massive star formation in the H I ridge region is likely to have been triggered by the galactic interaction, and thus studying the dust/gas ratios of the H I ridge region is important to identify such inflow gases from the SMC. One of the most reliable indicators of the dust column density is the near-infrared (NIR) dust extinction because it does not depend much on the dust temperature which is difficult to estimate since irrelevant components can be contaminated along the line of sight.

The method to evaluate the NIR dust extinction was originally introduced by Lada et al. (1994). In this method, the $H-K$ color excess is estimated from the mean $H-K$ color in a reference field (i.e., extinction-free region), which is so called Near-Infrared Color Excess (NICE) method. Lombardi & Alves (2001) developed the NICE method by combining the $H-K$ and $J-H$ colors, which is called the NICER (NICE revised) method. Furthermore, Dobashi et al. (2008) proposed the "X percentile metho". In this method, first, the colors are sorted from blue to red. Then the color excess is estimated from the difference between the X percentile of the color ($X = 0$–100%. $X = 100\%$ denotes the reddest star) and that of the reference field. The X percentile method has the advantage that it is less affected by the contamination of the foreground stars causing under-estimation of the dust extinction. By using these methods, NIR dust extinction maps in the LMC were constructed based on the 2MASS data (Imara & Blitz 2007 using the NICER method; Dobashi et al. 2008 using the X percentile method).

Furuta et al. (2019) derived the NIR dust extinction map of the LMC HI ridge region from the difference between the mean observed color and intrinsic colors accounting for several stellar spectral types. They compared the spatial distribution of the dust extinction with that of the hydrogen column density of different velocity components, and revealed differences in the dust/gas ratios between multiple velocity components, indicating that inflow gas from the SMC is present in the LMC H I ridge region. In addition, three-dimensional dust geometry was suggested based on the spatial (anti-)correlation between the dust extinction and hydrogen column density, which supported the gas collisions around 30 Dor. In this way, Furuta et al. (2019) demonstrated that the NIR extinction is a powerful tool to evaluate not only the dust/gas ratio but also dust geometry. However, the dust extinction estimated by Furuta et al. (2019) should be more or less under-estimated unless all the stars are located behind the clouds, because the color excess is calculated from the mean observed colors.

In this paper, we develop the method used in Furuta et al. (2019) by adopting the X percentile method to evaluate the dust extinction more precisely along the line of sight and to reveal the three-dimensional dust geometry. Using the resultant dust extinction map and gas maps of different velocity components, we discuss the dust distributions and dust/gas ratios of the multiple cloud components with different velocities.

2 The data

2.1 IRSF/SIRIUS point source catalog

We used the NIR (J, H and K_S bands) photometric catalog for the Magellanic Clouds (hereafter the IRSF catalog) obtained with the SIRIUS camera on the InfraRed Survey Facility (IRSF) 1.4 m telescope (Kato et al. 2007). In the IRSF catalog, Furuta et al. (2019) found systematic photometric errors due to the reflection of the incident twilight sky illumination inside the SIRIUS camera, and therefore reprocessed the raw data of the IRSF catalog by using the corrected flat-field images (for details of the analysis, see Furuta et al. 2019). In the present study, we selected data from this newly calibrated IRSF catalog according to the following criteria: (1) the magnitudes of the J, H and K_S bands are brighter than 18.8, 17.8 and 16.6 mag, respectively, corresponding to the 10σ limiting magnitudes of the original IRSF catalog, (2) "quality flag" in the original IRSF catalog is 1 in all the bands, indicating that the shapes of sources are "point like" and (3) the number of combined dithered images is larger than 8 in all the bands.

2.2 Sample selection

The IRSF catalog is contaminated with Galactic foreground stars, which causes under-estimation of the dust extinction. Thus, we identify stellar populations using a color-magnitude diagram (CM diagram) according to the method used in Furuta et al. (2019). The authors classi-

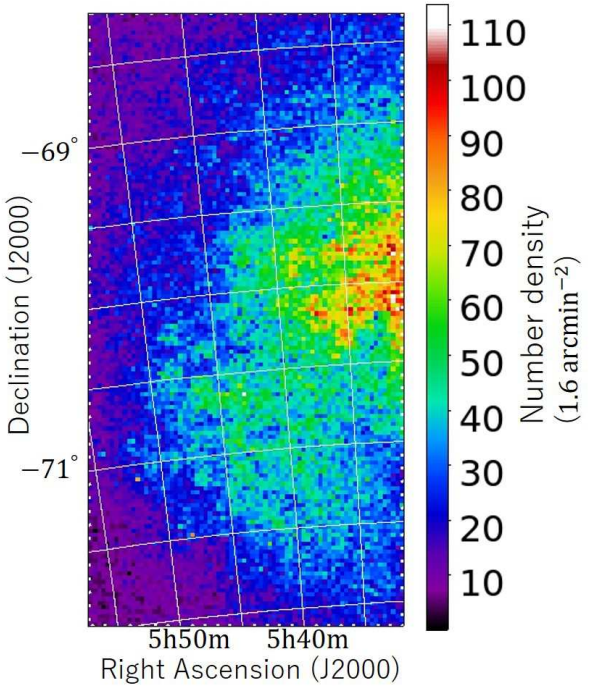


Fig. 1. Number density map of the selected sources of the LMC H I ridge region. The number of the stars included in each pixel of 1.′6×1.′6 is shown in the color scale.

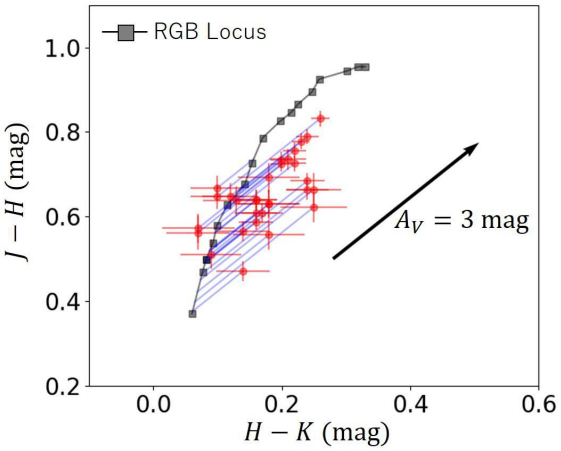


Fig. 2. Example of the color-color ($H-K$ vs. $J-H$) diagrams of the sources selected within a spatial bin of 1.′6×1.′6. Red circles and black squares are observed and intrinsic colors of RGB stars, respectively. The black arrow shows the reddening vector corresponding to $A_V = 3$ mag. Blue solid lines show the separation length between the observed and intrinsic colors of each star along the reddening vector.

fied stellar populations into three categories which mainly consist of main sequence stars, red giant branch (RGB) stars and Galactic foreground stars. The boundary lines between the three categories are determined on the CM diagram ($J-K$ vs. K) in their study. By using the same boundary lines, we classify the stellar populations, and use only the objects classified as RGB stars from the CM diagram. Figure 1 shows the number density map of the selected RGB stars in the H I ridge region.

3 Method

We describe our new method to measure the dust extinction along the line of sight in the LMC. The key is to take percentile values of the A_V distribution in each line of sight based on the X percentile method. In the following subsections, we explain our procedure step by step.

3.1 Measuring A_V for each star

We measure the dust extinction (A_V) for each star according to the method used in Furuta et al. (2019). In this method, A_V is calculated from the difference between the observed and intrinsic colors on a color-color diagram (CC diagram). In figure 2, we present a CC diagram ($H-K$ vs. $J-H$). The line connected with the black squares is the locus of the intrinsic colors of RGB stars (Bessell & Brett 1988). The black arrow in figure 2 is the reddening vector obtained from Cardelli, Clayton and Mathis (1989), which is determined by the NIR photometry in the Johnson system. To unify the photometric system, the observed and intrinsic colors are converted into the Johnson system according to the conversion equations suggested by Nakajima et al. (2005) and Elias et al. (1985). From the reddening law of Cardelli, Clayton and Mathis (1989), we have

$$A_V = 10.9E(J-H) \tag{1}$$

and

$$A_V = 13.2E(H-K), \tag{2}$$

where $E(J-H)$ and $E(H-K)$ are the color excess of the $J-H$ and $H-K$ colors, respectively. Using equations (1) and (2), we estimate A_V for each star from the separation length between the intrinsic and observed colors of each RGB star along the reddening vector on the CC diagram.

Some of the observed colors in figure 2 are bluer than the intrinsic colors. In this case, we assign negative extinction corresponding to the separation length between the observed and intrinsic colors. In case that no intersection point exists between the reddening vector and the locus of the intrinsic colors, "not a number" is assigned to the corresponding star.

3.2 Calculation of A_V distribution

For each spatial bin, we sort the stars with respect to their A_V values estimated in section 3.1. In figure 3a, we show

an example of the CC diagram of the stars included in a spatial bin of $5'\times5'$ at $(\alpha,\delta)_{\rm J2000.0} = (5^{\rm h}32^{\rm m},\ -69^\circ16')$. This spatial bin (the position is plotted in figures 12 and 15) is located in the LMC stellar bar region and has a low hydrogen column density ($<5\times10^{20}$ cm^{-2}). We select this region as an example for demonstrating the calculation of A_V distribution where we expect that no appreciable dust cloud is located along the line of sight.

The estimated A_V distribution in the bin is shown by the red histogram in figure 3b. To check the A_V distribution quantitatively, we plot individual A_V at every 5 stars as shown by the red circles in figure 3c. The slope of the A_V distribution in figure 3c indicates the presence of dust along the line of sight. However, even when there is no dust cloud along the line of sight, the slope is not zero due to the A_V scatter caused by photometric errors. To evaluate this effect, we simulate the A_V scatter based on the photometric errors as shown by the blue histogram and blue squares in figures 3b and 3c, respectively. As can be seen in the figures, the simulated A_V is scattered around zero due to the photometric errors, the distribution of which is quite similar to the observed A_V distribution. Therefore, we eliminate this effect from the observed data to evaluate the intrinsic dust distributions along the line of sight. In the following subsection, we describe the method to simulate the A_V scatter and to eliminate this effect.

3.3 A_V scatter caused by photometric errors

3.3.1 Calibration of the measured photometric errors

If the photometric errors in the IRSF catalog are over- or under-estimated for some reason, we cannot appropriately evaluate the A_V scatter caused by photometric errors. When photometric errors are appropriate values, the logarithm of χ^2/N should be close to zero for stars observed N times (e.g., Kaluzny et al. 1998; Yao et al. 2015). Here, χ^2 is defined as

$$\chi^2 = \sum^{N}\left(\frac{m-\bar{m}}{\sigma_{\rm m}}\right)^2, \tag{3}$$

where $\bar{m}$ is the weighted mean value of the colors of m observed N times for a star ($m = H-K$ or $J-H$), and σ_m is the photometric error. We calculate $\sigma_{H-K} = \sqrt{{\sigma_H}^2+{\sigma_K}^2}$ and $\sigma_{J-H} = \sqrt{{\sigma_J}^2+{\sigma_H}^2}$, where σ_J, σ_H and σ_K are the photometric errors of the J, H and K bands, respectively. By using the stars which are observed more than four times (i.e., $N>4$ in equation 3), we plot χ^2/N of the $H-K$ and $J-H$ colors as a function of their errors of σ_{H-K} and σ_{J-H} in figures 4a and 4b, respectively. From figures 4a and 4b, we see that χ^2/N becomes lower for higher σ_{H-K} and σ_{J-H}, showing that photometric errors are over-estimated for stars which have large photometric errors. Likely causes of the over-estimation are imperfect Point Spread Function (PSF) photometry, and/or over-estimation of the zero-point uncertainty. To solve this problem, we calculate the scaling factor F which is applied to σ_{H-K} and σ_{J-H}, following the method of Kaluzny et al. (1998).

More specifically, we binned the data of χ^2/N at an interval of 0.005 mag in both σ_{H-K} and σ_{J-H}. For each binned data at σ_{H-K} =0.018 to 0.103 mag and σ_{J-H} =0.016 to 0.046 mag, we calculate the scaling factor F so that the logarithm of χ^2/N becomes zero. Data points in figures 5a and 5b are the estimated scaling factors for each binned data of σ_{H-K} and σ_{J-H}, respectively. We finally perform the second-order polynomial fitting to the estimated scaling factors, and determine the scaling factor F as a function of photometric errors as shown by the solid lines in figures 5a and 5b. Figures 4c and 4d are the logarithmic plots of χ^2/N of the $H-K$ and $J-H$ colors, respectively, after applying the resultant scaling factor F to the photometric errors of each star. In the figures, we clearly see that the logarithm of χ^2/N are now closer to zero in all the range of photometric errors.

3.3.2 Simulation of the A_V scatter

In order to evaluate the A_V scatter caused by photometric errors in each spatial bin of $5'\times5'$, we perform a Monte Carlo simulation. We first generate a random set of colors for each star on the CC diagram in each bin assuming that the colors follow the two-dimensional Gaussian distribution, the center of which is fixed at the observed $H-K$ and $J-H$ colors. We here adopt the corrected σ_{H-K} and σ_{J-H} (see sub-subsection 3.3.1) as the standard deviation of the Gaussian distribution. We estimate A_V for each simulated star and subtract observed A_V from simulated A_V to exclude the dust extinction. The distribution of the simulated values are shown by the blue histogram and blue squares in figures 3b and 3c, respectively, which can be considered as the A_V scatter caused by photometric errors alone (i.e., without dust extinction) in the spatial bin. We repeat this simulation 100 times and generate 100 sets of the simulated A_V distribution for each spatial bin.

3.4 Extinction along the line of sight

In order to evaluate the intrinsic A_V distributions along the line of sight, we calculate the percentile values of A_V based on the X percentile method. In this method, A_V is originally estimated from the difference in the X percentile of the color between the reference and observed field, which

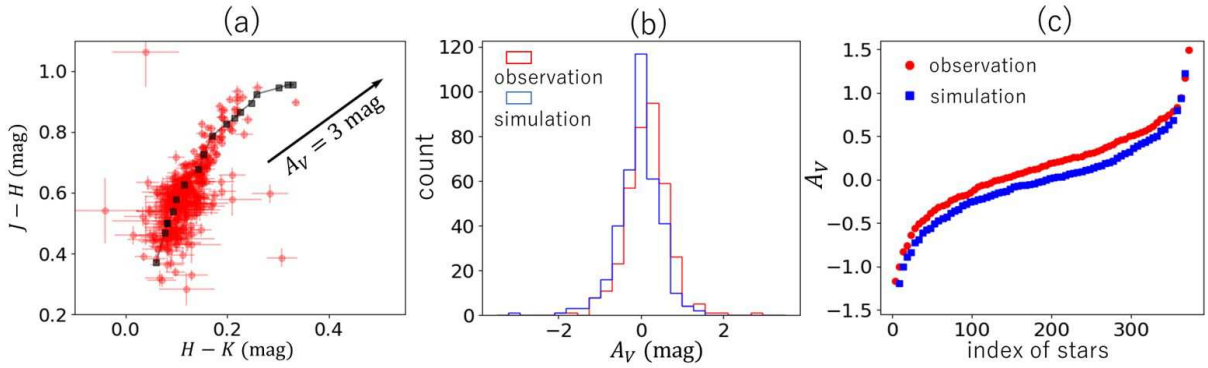


Fig. 3. (a) Color-color diagram ($H-K$ vs. $J-H$) of stars within a spatial bin of 5′ at $(\alpha, \delta)_{\rm J2000.0} = (5^{\rm h}32^{\rm m}, -69^\circ 16')$. (b) Histogram of observed (red) and simulated (blue) A_V values in the same region as in panel (a). (c) A_V distribution as a function of index of stars obtained from the same data as in panel (a). Red circles and blue squares are observed and simulated A_V plotted at every 5 stars, respectively.

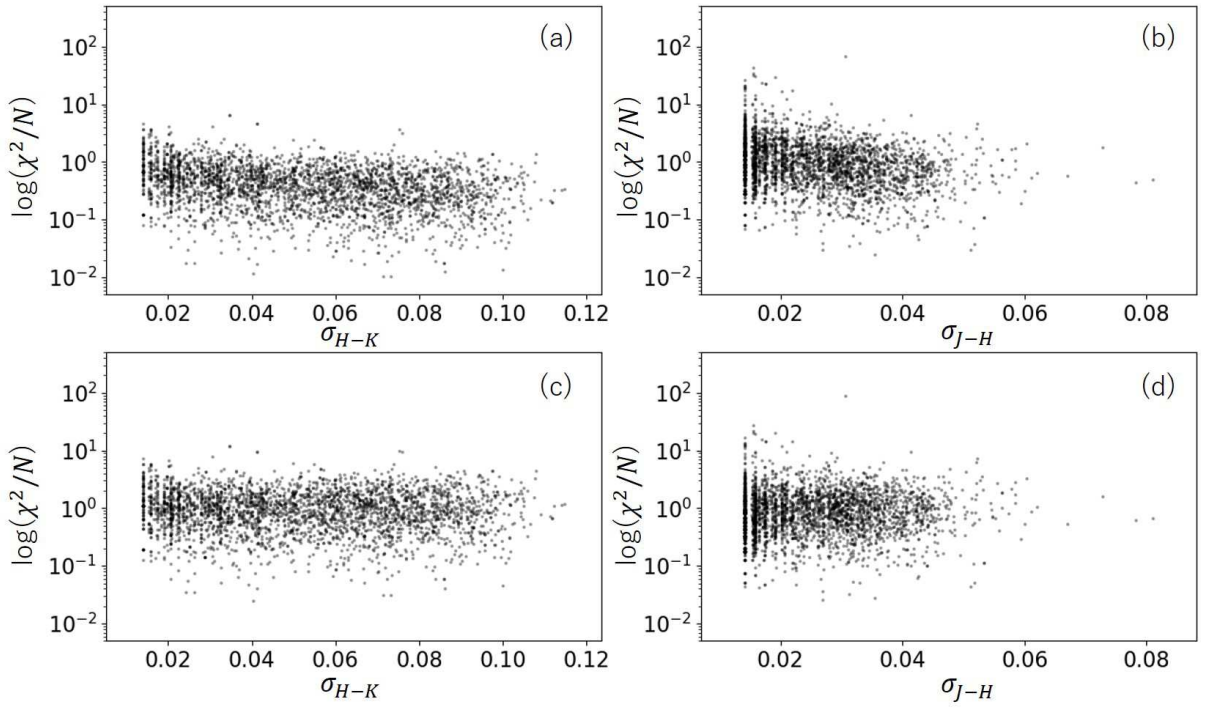


Fig. 4. Logarithmic plots of χ^2/N (defined by equation 3 in the text) vs. photometric errors of (a) the $H-K$ color and (b) the $J-H$ color for the stars in the present data which are observed more than four times. Panels (c) and (d) are the same diagrams as in panels (a) and (b), respectively, but those after re-scaling their photometric errors by applying the scaling factors F

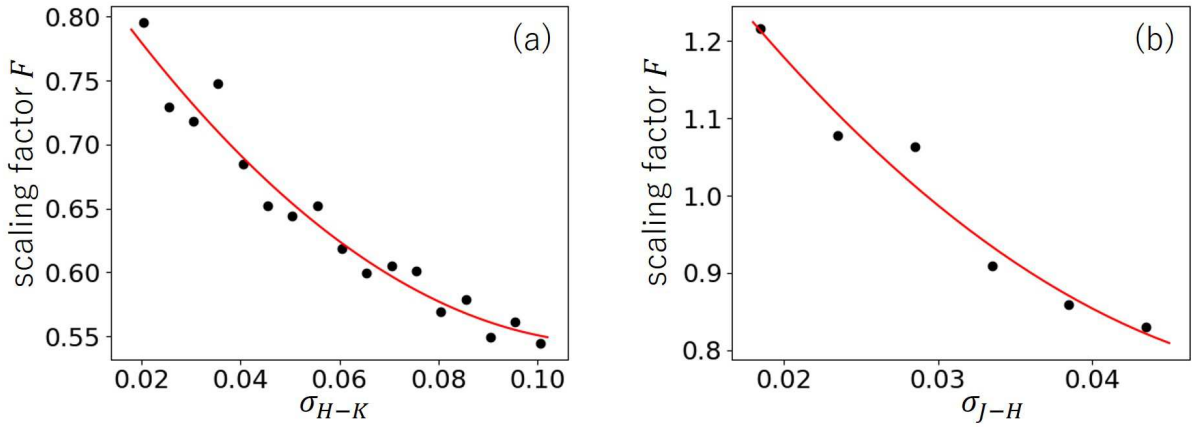


Fig. 5. Scaling factor F for the binned data of figures 4a and 4b as a function of photometric errors of (a) the $H-K$ color and (b) the $J-H$ color, respectively. Solid line represents the result of the second-order polynomial fitting.

enables us to infer the positions of dark clouds. In our study, we evaluate A_V at each percentile by subtracting simulated A_V (excluding dust extinction) from observed A_V (including dust extinction). We first average observed A_V in the range of X% to $(X+10)$% percentile in figure 3c, where X is 10% to 80% at every 10%. Red circles in figure 6a show the resultant mean observed A_V as a function of X%. We perform this procedure to the simulated A_V distribution and calculate the mean percentile values of A_V simulated 100 times as shown by blue squares in figure 6a. We finally calculate the difference between the observed and simulated percentile A_V at each percentile as shown in figure 6b. Here and hereafter, we define $A_V(X\%)$ as the resultant values shown in figure 6b (e.g., $A_V(10\%)$ is the mean A_V from 10% to 20% percentile of observed A_V after subtraction of simulated A_V). The uncertainties of $A_V(X\%)$ are calculated in subsection 3.5.

The shape of the histogram of the simulated A_V in figure 3b is consistent with that of the observed one, which demonstrates that our simulation using the scaling factor F works well. Indeed, $A_V(X\%)$ in figure 6b is almost constant value at 0.15 mag for all X%. The constant A_V is likely caused by the Galactic extinction across the LMC. Dobashi et al. (2008) find that the Galactic extinction is $A_V \simeq 0.2$ mag from the H I column density $N(\mathrm{H\,I})$, assuming $A_V/N(\mathrm{H\,I}) = 5.34\times10^{-22}$ mag/cm^{-2} (Bohlin et al. 1978, for R_V=3.1). In addition, the constant A_V for all X% in figure 6b means that the dust associated with the corresponding region of the LMC is not detected significantly along the line of sight as expected from the low column density region.

3.5 Uncertainties of dust extinction

We first calculate the A_V uncertainty of each star. When we perform the Monte Carlo simulation as described in subsection 3.3, the A_V value of each star is estimated 100 times. We estimate the A_V uncertainty of each star as the standard deviation of A_V simulated 100 times. As a next step, we calculate the uncertainties in the mean values of A_V included in X% to $(X+10)$% percentile, $\sigma_{A_{V,X}}$, as

$$\sigma_{A_{V,X}} = \frac{1}{N_X}\sqrt{\sum_{i=1}^{N_X}\delta A_{Vi}^2}, \tag{4}$$

where N_X and δA_{Vi} are the number of stars included in X% to $(X+10)$% percentile, and the A_V uncertainty of the ith star, respectively. $\sigma_{A_{V,X}}$ for each X% is shown in figure 6b as error bars.

When we compare $A_V(X\%)$ with the hydrogen column density to evaluate detailed dust geometry (section 5), we additionally consider the uncertainty of the percentile virtually corresponding to the uncertainty of the distance along the line of sight by using a simple count uncertainty (i.e., $\sqrt{N}$). We calculate its uncertainty as $\sigma_{d,X} = (A_{Vk} - A_{Vl})/2$, where A_{Vk} and A_{Vl} are the A_V values for the stars of the index of k and l defined as the integer part of $(i_{\mathrm{center}} + \sqrt{N})$ and $(i_{\mathrm{center}} - \sqrt{N})$, respectively. Here, i_{center} is the median index of stars included in X% to $(X+10)$% percentile, and N is the total number of stars in the spatial bin. We finally calculate the total uncertainties of $A_V(X)$% from the error propagation, $\delta A_V(X\%) = \sqrt{\sigma_{A_{V,X}}^2 + \sigma_{d,X}^2}$.

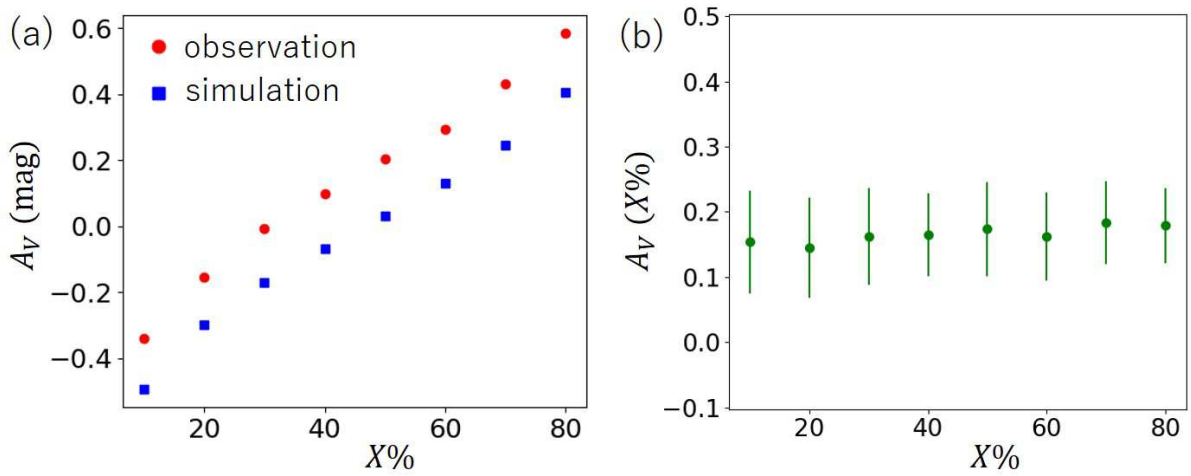


Fig. 6. (a) Mean A_V in the range of X% to $(X+10)$% percentile of A_V distribution in figure 3c for X=10% to 80% at every 10%. (b) Difference between observed and simulated A_V at each percentile shown in panel (a).

4 Result

4.1 Results for the individual lines of sight

The results for two example lines of sight are presented in figures 7 and 8 for the spatial bins of $5'\times5'$ centered at $(\alpha,\delta)_{\rm J2000.0} = (5^{\rm h}38^{\rm m}, -69^\circ10')$ in 30 Dor and $(5^{\rm h}32^{\rm m}, -68^\circ28')$, respectively (the positions of these regions are plotted in figures 12 and 15). In the former region, gas collision is suggested and thus the dust cloud is expected to be located in front of the LMC disk (Furuta et al. 2019). In the latter region, there is relatively high column density gas of the LMC disk (see figure 12c), and the gas collision is not suggested.

In figure 7a, we recognize that the observed A_V histogram is shifted to positive values and broader compared to the simulated one. $A_V(10\%)$ of about 1.1 mag in figure 7c suggests that the dust cloud is located in front of almost all stars as expected from the gas colliding region and largely contribute to the dust extinction in this region. In addition, the broader A_V histogram is likely to be caused by the diffuse extinction existing along the line of sight. The former trend is also suggested by Tatton et al. (2013) who estimated A_V for each star around 30 Dor using a CM diagram ($J-K$ vs. K) and found that almost all the stars around the region have large dust extinction ($A_V > 1.2$ mag).

In figure 8a, we find two peaks around A_V=0.0 mag and 1.0 mag in the observational histogram. $A_V(10\%)$ of 0.2 mag in figure 8c is consistent with the Galactic foreground extinction, which suggests that the first peak in the A_V histogram is attributed to stars not affected by the dust extinction in the LMC itself. On the other hand, the second peak of the A_V histogram is likely attributed to stars behind the dust cloud in the LMC, causing a rapid increase of A_V at X=30% and onward in figure 8c. This result is consistent with the existence of the high column density gas of the LMC disk.

4.2 Extinction map along the line of sight

In this subsection, we consider large-scale dust geometry. Figure 9 shows the $A_V(10\%)$ to $A_V(80\%)$ maps in the H I ridge region. As described in section 3, A_V is calculated with $5'\times5'$ bins every $1'.6$ grid and thus the PSF of the A_V map is of a rectangular shape with the spatial resolution of $5'$ and the grid size of $1'.6$. Since $A_V(X\%)$ is the cumulative dust extinction from an observer to X%, A_V increases with X% as can be seen in the figure. The $A_V(80\%)$ map is considered to trace almost all the dust in the LMC. We present the uncertainty map of each A_V map in figure 10. The uncertainty is relatively large in the east of the H I ridge region due to the lower density of stars (see figure 1).

In order to evaluate the Galactic foreground extinction using the derived dust extinction map, we calculate the averaged A_V in the $A_V(10\%)$ map where the total hydrogen column density N(H) is lower than 5.0×10^{20} cm^{-2} (the total hydrogen column density is defined in the next subsection). As a result, we obtain 0.15 mag, which is consistent with the foreground extinction towards the LMC ($\sim$ 0.2 mag) estimated by Dobashi et al. (2008).

We compare the derived A_V map with the previous one in Furuta et al. (2019). Since the previous A_V map was estimated from the mean observed colors, we use the $A_V(40\%)$ map (i.e., mean A_V from 40% to 50% percentile A_V) for comparison after subtracting the Galactic foreground extinction. Figures 11a and 11b show the $A_V(40\%)$

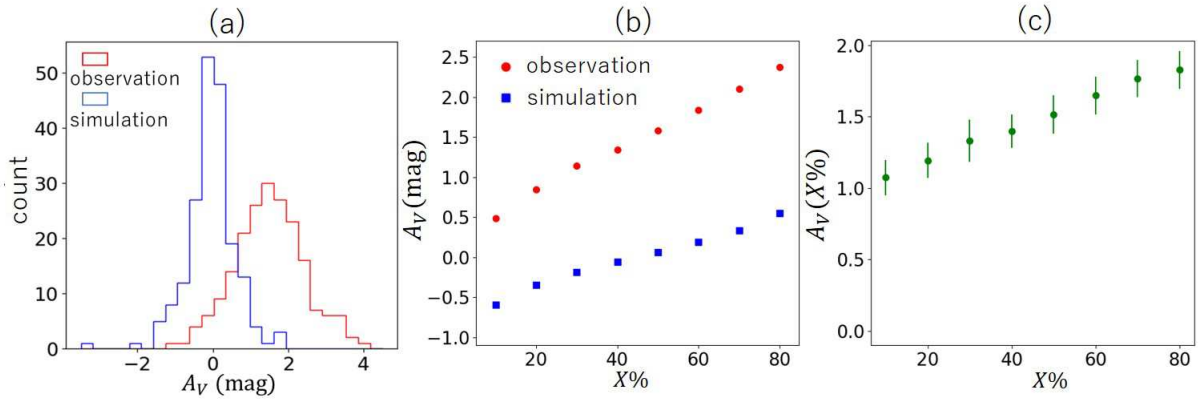


Fig. 7. (a) Histogram of observed (red) and simulated (blue) A_V for the spatial bin of $5' \times 5'$ centered at $(\alpha, \delta)_{\mathrm{J2000.0}} = (5^{\mathrm{h}}38^{\mathrm{m}}, -69^{\circ}10')$ in 30 Dor. Panels (b) and (c) are the same diagram as in figures 6a and 6b, respectively, but corresponding to panel (a).

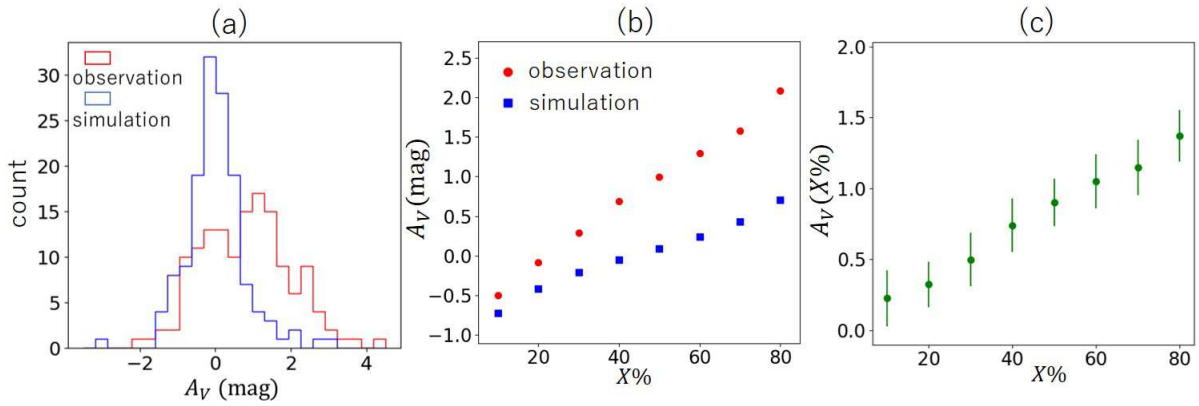


Fig. 8. Same diagrams as in figure 7 but for the spatial bin of $5' \times 5'$ centered at $(\alpha, \delta)_{\mathrm{J2000.0}} = (5^{\mathrm{h}}32^{\mathrm{m}}, -68^{\circ}28')$.

map and our previous A_V map, respectively, whose spatial resolution is reduced to be the same as that of the $A_V(40\%)$ map. Figure 11c shows the $A_V(40\%)$ map after subtraction of the previous map, from which we confirm that the $A_V(40\%)$ map is consistent with the previous A_V map, although local differences can be seen at high extinction regions.

5 Comparison of dust extinction with N(H)

5.1 Gas tracer

As an atomic gas tracer, we use the H I velocity-integrated intensity maps constructed by Fukui et al. (2017) and Tsuge et al. (2019), where the Australia Telescope Compact Array (ATCA) and Parkes H I 21 cm data (Kim et al. 2003) are used. They subtracted the galactic rotation velocity from the H I data, which is defined as V_{offset}, and decomposed the H I map into three velocity components (see Tsuge et al. 2019 for details of the analysis). These velocity components are defined as the L-, I- and D-components with the integrated velocity ranges of $V_{\mathrm{offset}} = -100$ to -30, -30 to -10 and -10 to 10 km s^{-1}, respectively. A typical H I spectrum in the H I ridge region is shown in figure 1 of Tsuge et al. (2019) together with the velocity range of each velocity component (see also figure 8 of Tsuge et al. 2021 for examples of the H I spectra in the LMC H I ridge region). The L-, I- and D-components are named after the initial letters of "Low", "Intermediate" and "Disk" velocity, respectively. As a molecular gas tracer, we use the rotational transitions of ^{12}CO (J =1–0) observed with the NANTEN 4 m telescope (Fukui et al. 1999). The CO integrated intensity map is decomposed into the L-, I- and D-components according to the above velocity ranges of the H I integrated intensity maps.

The H I integrated intensity map is converted into the H I column density map by using the conversion factor, $X_{\mathrm{H\,I}} = 1.82 \times 10^{18}$ cm^{-2}/(K km s^{-1}) (Dickey & Lockman 1990). CO is used to trace H_2 through the CO-to-H_2 conversion factor, X_{CO}. We reduce the spatial resolutions of the H I column density maps and CO maps to be the same as that of the A_V map at a resolution of $5'$ by convolving

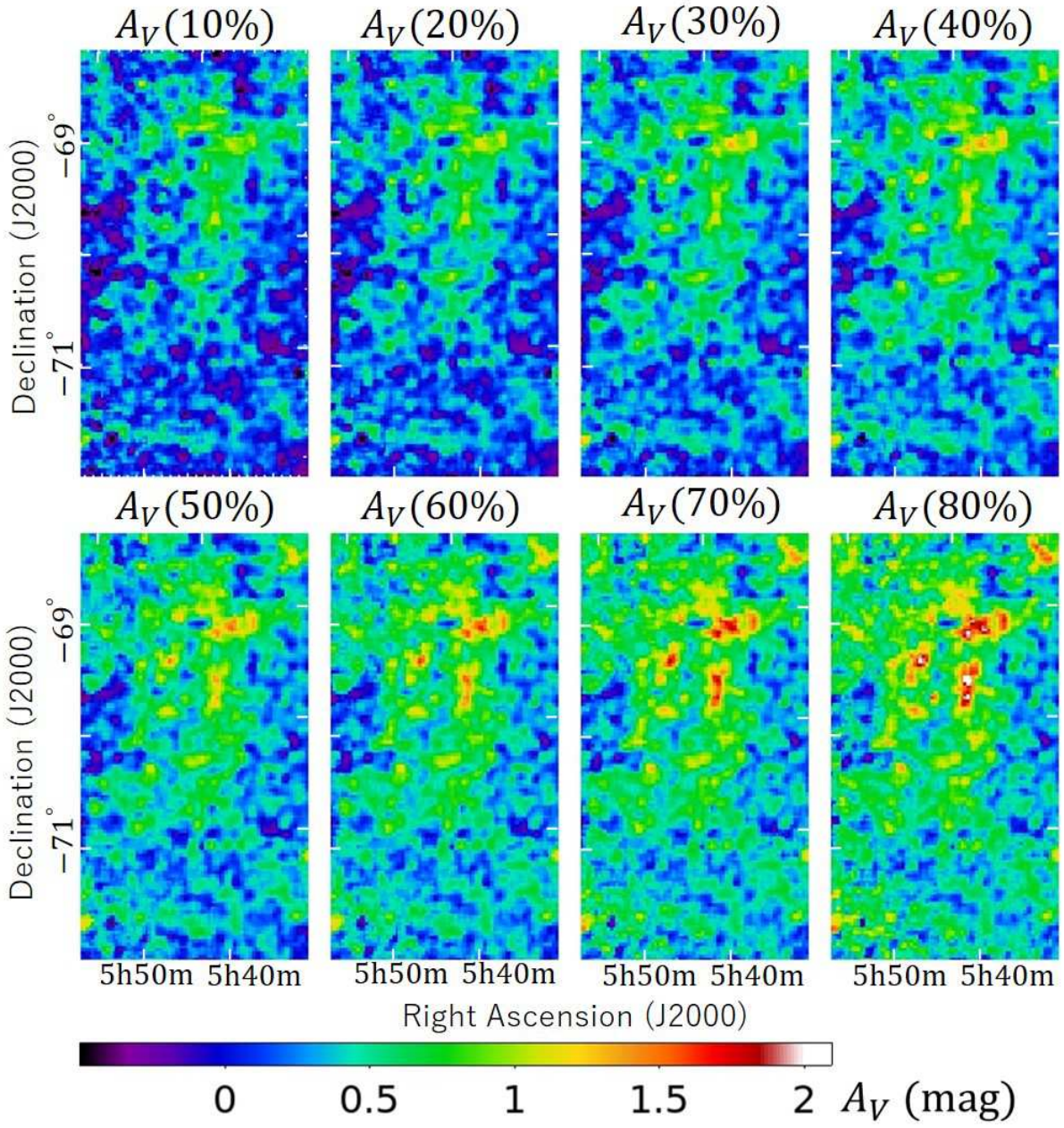


Fig. 9. Cumulative dust extinction map from an observer to stars included in X% to $(X+10)$% percentile for X=10% to 80% at every 10%. The angular resolution of the maps is 5′.

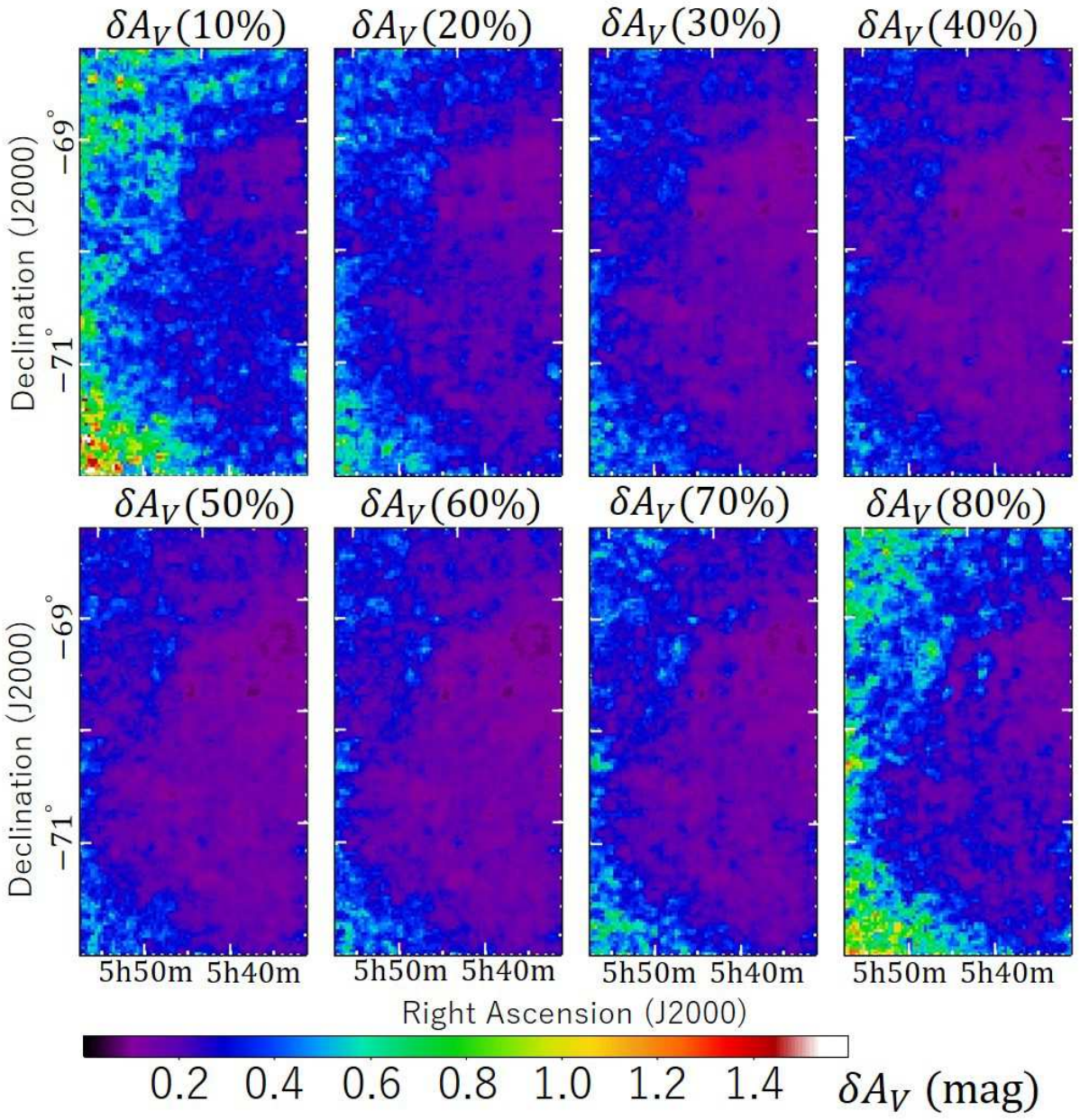


Fig. 10. Uncertainties of the dust extinction maps shown in figure 9.

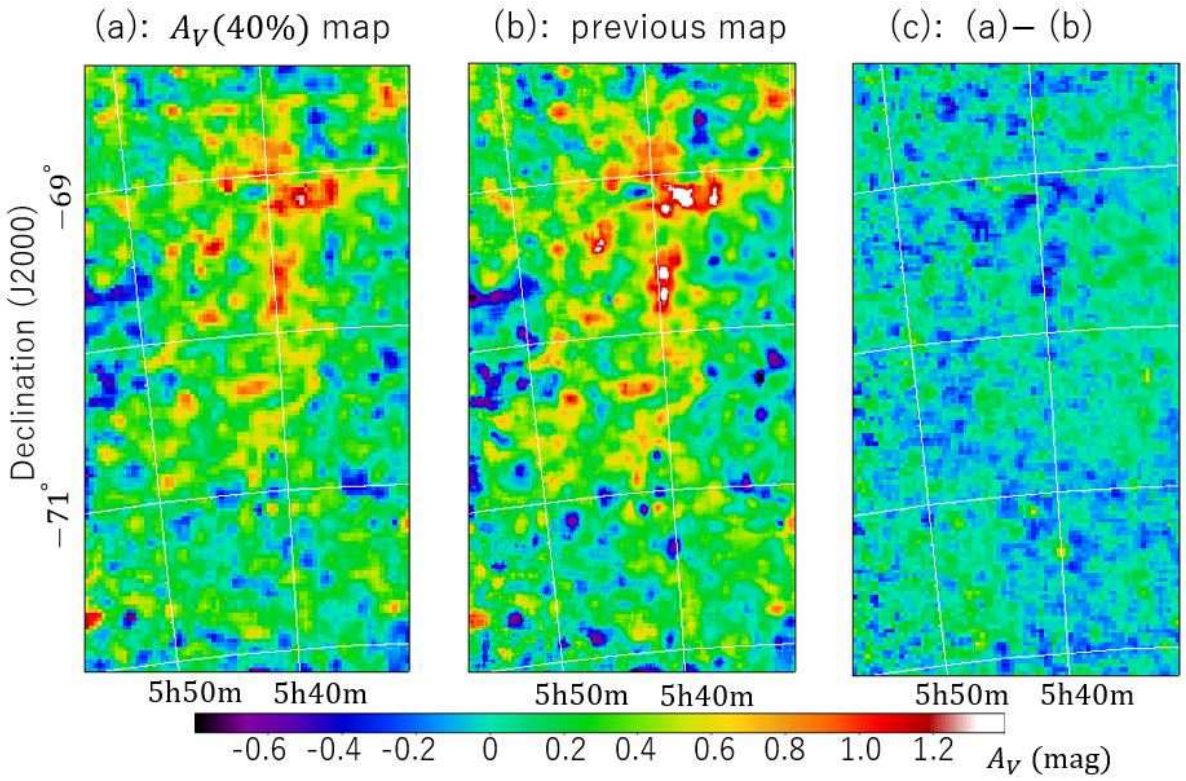


Fig. 11. (a) A_V(40%) map derived in this paper. (b) Mean A_V map derived from Furuta et al. (2019). The Galactic foreground extinction is subtracted in both panels (a) and (b). (c) Difference in A_V between panels (a) and (b).

with a boxcar kernel of $5' \times 5'$. Thus the PSF of the gas maps is of the same rectangular shape with that of the A_V map to make a comparison on a pixel-by-pixel basis (subsection 5.3). We calculate the total gas column density N(H) of each of the L-, I- and D-component as

$$N(\mathrm{H}) = N(\mathrm{H\,I}) + 2N(\mathrm{H_2}), \tag{5}$$

where N(H I) and $N(\mathrm{H_2})$ are the H I and the $\mathrm{H_2}$ column densities, respectively.

5.2 A_V vs. N(H) correlation

To check the spatial correlation between A_V and N(H), we present the A_V(80%) maps with the contours of N(H) of the L-, I- and D-components in figure 12. Here, we adopt $X_{\mathrm{CO}} = 7 \times 10^{20}$ cm^{-2}/(K km s^{-1}) which is the averaged X_{CO} in the LMC derived from Fukui et al. (2008). Because N(H) is the integrated value along the line of sight, the A_V(80%) map is expected to correlate with the N(H) maps best among the A_V(10%) to A_V(80%) maps. Indeed, the I- and D-component gases correlate well with the dust extinction. On the other hand, the L-component correlates well with the dust extinction in the northern part but not in the southern part, as can be seen from figure 12a. This trend can also be seen in Furuta et al. (2019), who consider the gas distribution based on the scenario that the L-component gas is falling into the LMC disk and the collision is on-going in the H I ridge region (Fukui et al. 2017).

5.3 Decomposition of A_V into different velocities

We estimate the fractions of A_V due to the dust associated with the L-, I- and D-components for every percentile from 10% to 80%, applying the fitting method described in Furuta et al. (2019) to our newly constructed A_V maps. The fitting function is expressed as the following equation:

$$A_V = \theta(y - y_0)\, aN(\mathrm{H})_{\mathrm{L}} + bN(\mathrm{H})_{\mathrm{I}} + cN(\mathrm{H})_{\mathrm{D}}, \tag{6}$$
$$\theta(y - y_0) = \begin{cases} 1 & (y \geq y_0), \\ 0 & (y < y_0), \end{cases}$$
$$N(\mathrm{H})_k = N(\mathrm{H\,I})_k + 2x_k W(\mathrm{CO})_k \ (k = \mathrm{L,\ I\ or\ D}),$$

where a, b and c are the free parameters indicating the dust/gas ratios (i.e., A_V/N(H)) of the L-, I- and D-components, respectively, while $N(\mathrm{H})_k$ for k=L, I or D is the gas column density of the L-, I- or D-component. Here, y and y_0 are the pixel coordinates along the Declination direction. $\theta(y - y_0)$ is a step function and the free parameter y_0 indicates that the L-component at $y > y_0$ is located in front of the LMC disk, contributing to the dust extinc-

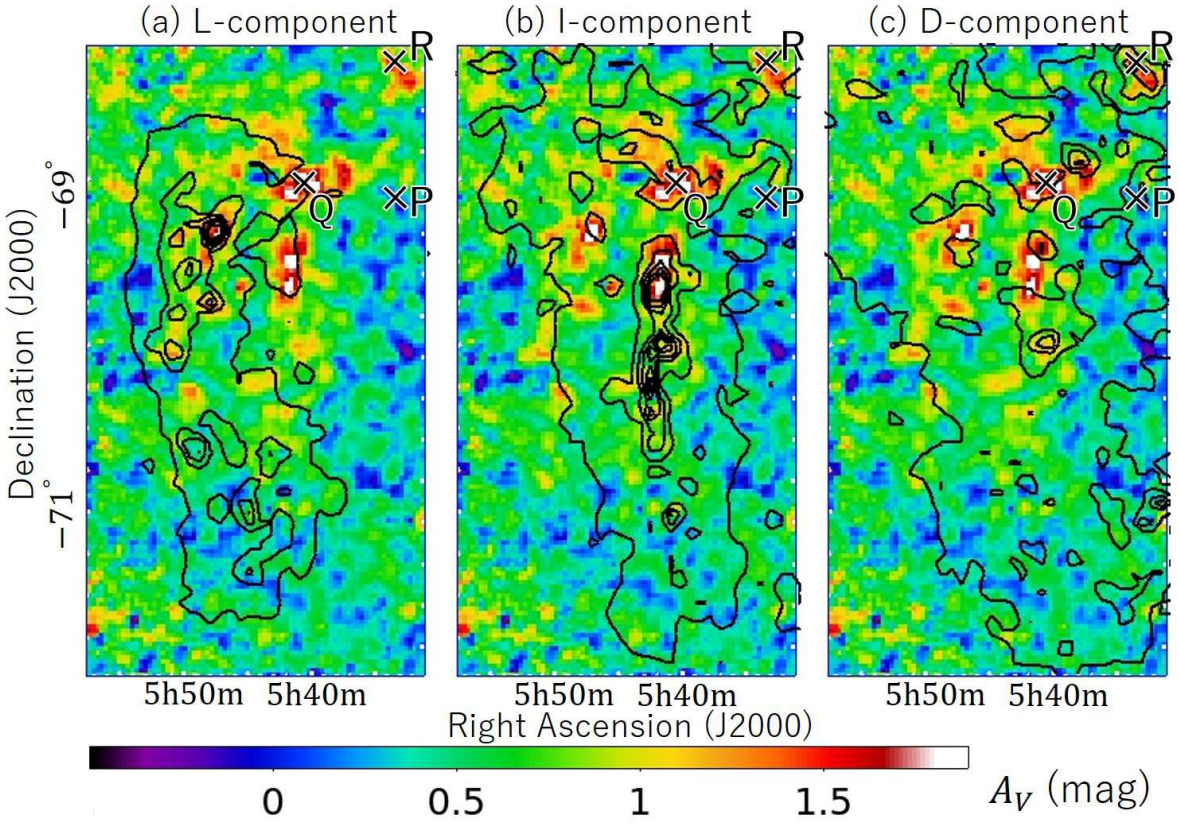


Fig. 12. A_V(80%) map superposed on the N(H) contour maps of the (a) L-, (b) I- and (c) D-component assuming $X_{\rm CO} = 7 \times 10^{20}$ cm^{-2}/(K km s^{-1}). The contour levels are (0.6, 2.1, 3.6, 5.0, 6.5 and 8.0)$\times 10^{21}$ cm^{-2}. The cross symbols labeled "P", "Q" and "R" show the positions of the spatial bins where the plots in figures 3, 7 and 8, respectively, are created.

tion, whereas the L-component at $y < y_0$ is located behind the LMC disk, not contributing to the dust extinction (see figure 7 of Furuta et al. 2019). For simplicity, we assume that the boundary is parallel to the Right Ascension direction. $N({\rm H\,I})_k$ and $W({\rm CO})_k$ are the H I column density and the integrated CO intensity of each velocity component, respectively. x_k is the free parameter corresponding to $X_{\rm CO}$ of the L-, I- or D-component. We set the $X_{\rm CO}$ factor of each velocity component as a free parameter because Furuta et al. (2019) revealed that $X_{\rm CO}$ of each velocity component is significantly different from each other.

As demonstrated by Furuta et al. (2019), we can decompose A_V into the three different velocity components with the linear regression of equation (6) using $\delta A_V(X\%)$ calculated in subsection 3.5. In this study, we newly apply this method to each $A_V(X\%)$ map after subtraction of the Galactic foreground extinction, which enables us to decompose A_V existing along the line of sight into different velocity components. In other words, we can evaluate the three-dimensional dust geometry associated with the L-, I- and D-components. We discuss the dust geometry and dust/gas ratios of them in the next section.

When we perform the linear regression, we use only the region where $N({\rm H})_{\rm D}$ is higher than 1.0×10^{20} cm^{-2} assuming $X_{\rm CO} = 7 \times 10^{20}$ cm^{-2}/(K km s^{-1}). In addition, we mask the 30 Dor region where the surface brightness is higher than 20 MJy/sr in the Spitzer/MIPS 24 μm map from the SAGE program (Meixner et al. 2006), because De Marchi & Panagia (2014) suggested that the reddening law around the 30 Dor region does not follow that of Cardelli, Clayton and Mathis (1989), which causes the under-estimation of the dust/gas ratio around 30 Dor.

The resultant fitting parameters (y_0, a, b, c and x_k) are summarized in table 1. The uncertainties of the free parameters are estimated by the formal regression errors using the A_V uncertainties. We plot A_V/N(H) and $X_{\rm CO}$ thus obtained for each velocity component and those derived from Furuta et al. (2019) as a function of $X\%$ in figures 13a and 13b, respectively.

Table 1. Fitting parameters derived from comparison of the dust extinction and $N(\mathrm{H})$ of each component.

Name	Reduced χ^2	y_0*	$a\left(\frac{A_V}{N(\mathrm{H})}\right)^\dagger$ (L-component)	$x_\mathrm{L}\ (X_\mathrm{CO})^\ddagger$ (L-component)	$b\left(\frac{A_V}{N(\mathrm{H})}\right)^\dagger$ (I-component)	$x_\mathrm{I}\ (X_\mathrm{CO})^\ddagger$ (I-component)	$c\left(\frac{A_V}{N(\mathrm{H})}\right)^\dagger$ (D-component)	$x_\mathrm{D}\ (X_\mathrm{CO})^\ddagger$ (D-component)
$A_V(10\%)$	0.51	$-69.^\circ4\pm0.^\circ1$	1.13 ± 0.24	2.6 ± 2.1	1.26 ± 0.16	1.1 ± 0.7	0.35 ± 0.13	8.1 ± 6.5
$A_V(20\%)$	0.91	$-69.^\circ4\pm0.^\circ1$	0.91 ± 0.23	4.1 ± 2.6	1.31 ± 0.15	1.1 ± 0.6	0.59 ± 0.13	3.8 ± 3.2
$A_V(30\%)$	1.21	$-70.^\circ9\pm0.^\circ2$	0.46 ± 0.12	8.0 ± 4.5	1.29 ± 0.15	0.6 ± 0.6	0.87 ± 0.12	3.1 ± 2.1
$A_V(40\%)$	1.37	$-70.^\circ9\pm0.^\circ2$	0.54 ± 0.11	8.1 ± 3.5	1.35 ± 0.15	0.5 ± 0.5	1.16 ± 0.12	2.2 ± 1.5
$A_V(50\%)$	1.44	$-70.^\circ9\pm0.^\circ2$	0.77 ± 0.11	4.9 ± 2.2	1.21 ± 0.15	0.7 ± 0.6	1.56 ± 0.12	1.5 ± 1.1
$A_V(60\%)$	1.40	$-70.^\circ9\pm0.^\circ2$	0.94 ± 0.12	4.4 ± 2.0	1.23 ± 0.15	0.4 ± 0.6	1.83 ± 0.12	1.2 ± 1.0
$A_V(70\%)$	1.26	$-70.^\circ9\pm0.^\circ2$	1.10 ± 0.12	4.8 ± 1.8	1.21 ± 0.16	0.9 ± 0.7	2.05 ± 0.13	1.0 ± 0.9
$A_V(80\%)$	0.80	$-70.^\circ9\pm0.^\circ2$	1.24 ± 0.13	5.3 ± 1.8	1.36 ± 0.17	1.2 ± 0.7	2.08 ± 0.14	1.7 ± 1.0
previous map$	1.16	$-70.^\circ8\pm0.^\circ2$	0.71 ± 0.08	6.8 ± 1.6	1.35 ± 0.11	1.5 ± 0.4	1.10 ± 0.12	2.8 ± 1.0

* The boundary position of y_0 in the units of pixel is converted into $\delta_{\mathrm{J2000.0}}$ at $\alpha_{\mathrm{J2000.0}}=87.^\circ4$

† Given in the units of 10^{-22} mag/(H cm^{-2})

‡ Given in the units of 10^{20} cm^{-2}/(K km s^{-1})

$ Furuta et al. (2019) allowing the X_CO factors of the L-, I- and D-components to vary.

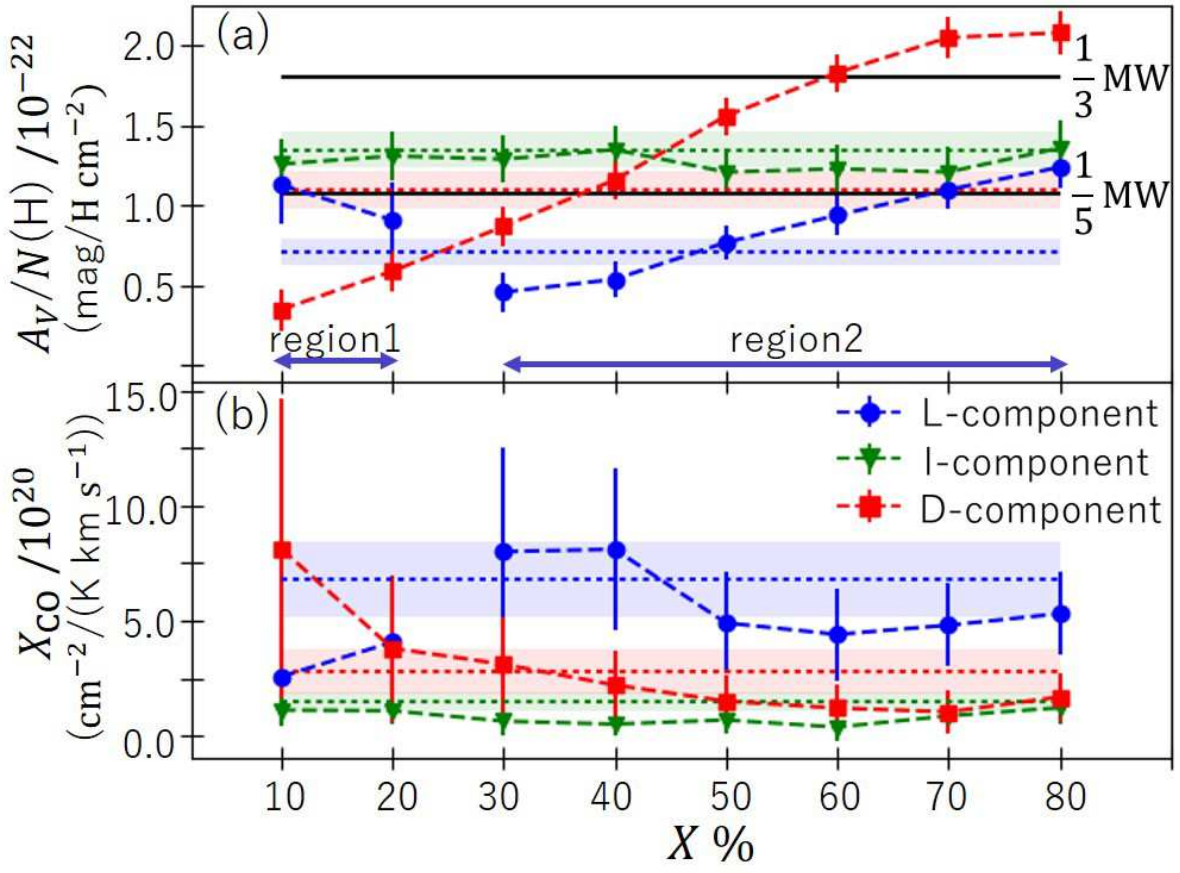


Fig. 13. Fitting parameters of (a) $A_V/N(\mathrm{H})$ and (b) X_CO derived from the linear regression of equation (6) as a function of X%. Circles, triangles and squares are the parameters derived for the L-, I- and D-components, respectively. Data points and dotted lines are color-coded according to their velocity components. Dotted horizontal lines and shaded regions show the parameter of each velocity component and 1σ level spread around the parameter, respectively, derived from Furuta et al. (2019). In panel (a), solid horizontal lines correspond to 1/3 and 1/5 of $A_V/N(\mathrm{H})$ in the Milky Way (MW). "region 1" and "region 2" are part of the L-component separated by the derived boundary positions of y_0 (see subsection 6.1).

6 Discussion

6.1 Large-scale dust geometry

We consider the dust geometry of the L, I and D-components, based on the results of the linear regression fitting. As shown in table 1, the estimated boundary positions of y_0 at $\alpha_{\rm J2000.0}$ =87.°4 are $\delta_{\rm J2000.0} = -69.°4 \pm 0.°1$ for the maps of $A_V(10\%)$ and $A_V(20\%)$, while $\delta_{\rm J2000.0} = -70.°9 \pm 0.°2$ for the maps of $A_V(30\%)$ to $A_V(80\%)$, both of which are denoted by the horizontal lines in figure 14a. Here, we name the former and latter boundaries boundary 1 and boundary 2, respectively, and the three regions separated by boundaries 1 and 2 as regions 1 to 3 (figures 13a and 14b). The position of boundary 2 is consistent with that obtained by Furuta et al. (2019) using the averaged A_V map (see table 1). We newly find the presence of boundary 1 owing to our new method evaluating the dust distribution along the line of sight. The resultant two boundary positions indicate that the L-component in region 1 is located from observers to X=20%, while the L-component in region 2 is located on the far side from X=20%. In addition, the L-component in region 3 is located behind the LMC.

Furuta et al. (2019) only revealed that the L-component in region 3 is behind the LMC disk. The present study enables us to evaluate the three-dimensional geometry of the L-, I- and D-components using A_V/N(H) for each X%. Note that A_V in figure 13a is an integrated value towards X% (i.e., variable depending on X%), while N(H) is a constant value integrated over the entire range along the line of sight. Thus, in principle, A_V/N(H) increases more or less with X% for a given line of sight. However, since the decomposition of A_V to each velocity component is determined by the fitting, A_V/N(H) can decrease with X% (e.g., the decrease in A_V/N(H) of the L-component within the errors from X=10% to 20%).

Using A_V/N(H) for each X% and the boundary positions of the L-component, we suggest the geometry of each velocity component as illustrated schematically in figure 14b. First, A_V/N(H) of the D-component monotonically increases with X% in figure 13a, which indicates that the D-component (i.e., Disk component) is extended along the line of sight as shown by the red rectangle in figure 14b. This trend is consistent with a general hypothesis that stars in the LMC are mixed with the LMC gas. On the other hand, A_V/N(H) of the I-component is constant within the errors over the integration range in figure 13a, which implies that dust in the I-component is located in front of almost all the stars in the LMC as shown by the green clouds in figure 14b.

A_V/N(H) of the L-component from X=30% to 80% increases with X% as can be seen in figure 13a, which indicates that the L-component in region 2 is extended from $X = 30\%$ to $X = 80\%$. On the other hand, A_V/N(H) of the L-component at X=10% and 20% is constant within the errors, which is the same trend as the I-component, indicating that region 1 is located in front of almost all the stars. The significant decrease in A_V/N(H) of the L-component from $X = 20\%$ to 30% is caused by the change of y_0 in equation 6, i.e., the difference of the N(H) distribution used for the fitting. The expected geometry of the L-component is shown by the blue disk in figure 14b, suggesting that the L-component is penetrating the LMC disk at region 2, and is decelerating through interaction with the D-component, which causes the I-component (i.e., intermediate velocity) located in front of almost all the stars in the LMC. 30 Dor and N159 are expected to be located behind the I-component as shown in figure 14b, whereas 30 Dor and N159 in figure 12b show good spatial correlation with the I-component. Since the I-component is considered to be evidence for gas collision, their spatial correlation supports that the massive star formation in these region may have been triggered by collisions of the LMC disk with clouds as seen in the I-component (Fukui et al. 2017, 2019; Tokuda et al. 2019).

The geometry in figure 14b suggests that gas collision occurred in the north region prior to the south region. In order to verify such a difference in the timing of the gas collision, we compare the evolutionary stages of giant molecular clouds (GMCs) with the crossing timescale of the gas collision. Kawamura et al. (2009) classified GMCs in the LMC into four evolutionary stages, Type I–Ⅲ and last stage (Type I is the youngest phase). They found the evolutionary sequence from the south (young) to the north (old) of the H I ridge region, i.e., Type-I GMCs in region 3, Type-Ⅲ GMCs around N159 and last-stage GMCs near 30 Dor. The transition timescale from Type I to last stage is $\sim$ 25 Myr. Assuming that the velocity of the inflow gas (L-component) is 100 km/s and the thickness of the LMC disk is 2 kpc (Balbinot et al. 2015), it spends 20 Myr for the inflow gas to cross the LMC disk, which is consistent with the transition timescale ($\sim$ 25 Myr) from Type-I GMCs in region 3 to last-stage GMCs near 30 Dor. Therefore, the colliding cloud geometry shown in figure 14b can reasonably explain the evolutionary sequence in the H I ridge region found by Kawamura et al. (2009).

6.2 Comparison of dust extinction with dust emission

In order to check the validity of the geometry that the L-component in region 3 is located behind the LMC disk, we compare the dust extinction with the dust emission;

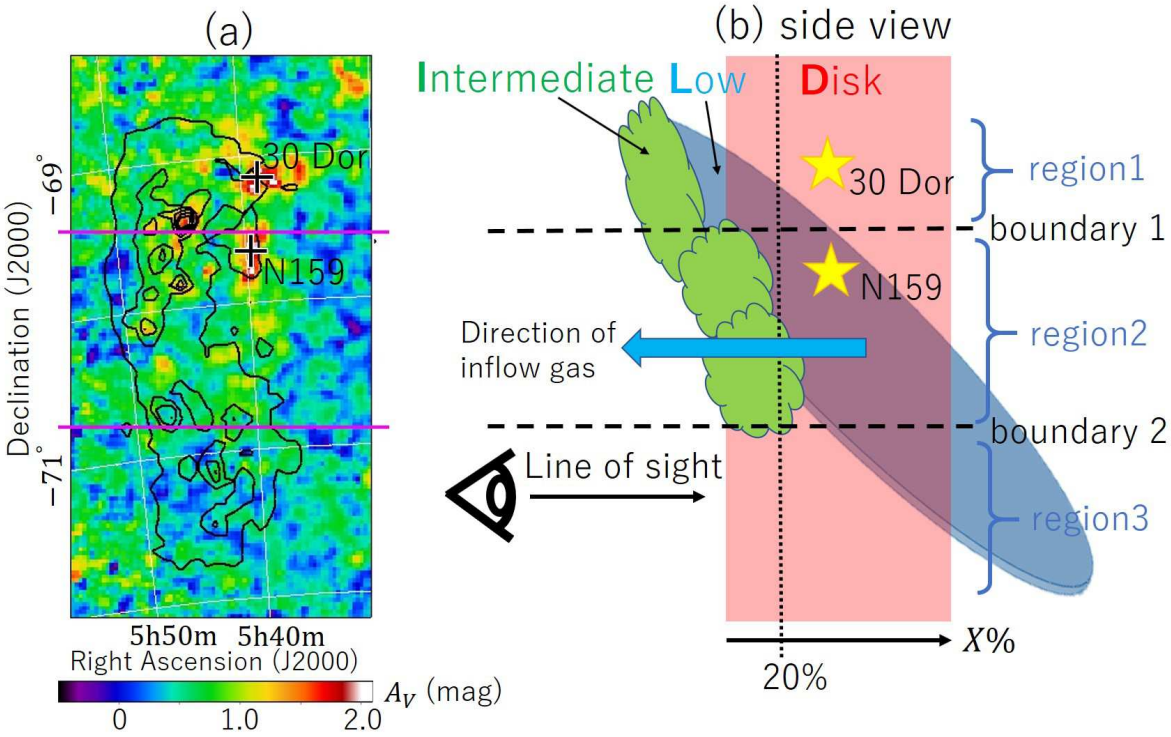


Fig. 14. (a) A_V(80%) map superposed on the same contours of the L-component as in figure 12a. Magenta horizontal lines show the estimated boundary positions of the L-component. (b) An illustration of the side view of the expected distributions of the L-, I- and D-components. Red rectangle and blue disk denote the LMC gas (D-component) and an inflow gas from outside the LMC (L-component), respectively. Green clouds are the I-component affected by the interaction between the L- and D-components.

the dust extinction is caused by only the dust in front of the stars while the emission can come from all dust. As a dust emission map, we use the map of the dust optical depth at 353 GHz, τ_{353}, obtained from the Planck and IRAS far-infrared data (Planck Collaboration 2014). To estimate τ_{353} in the LMC, Tsuge et al. (2019) calculated the Galactic foreground dust optical depth from the foreground H I intensity (W(H I)) using the conversion factor from W(H I) to τ_{353} derived from Fukui et al. (2015). We use the τ_{353} map after subtraction of the foreground component.

Figure 15a shows the τ_{353} map with the contours of A_V(80%) detected with significance higher than 1σ and $A_V \geq 0.6$ mag, from which we find that the dust emission exists in region 3 while the dust extinction does not. In regions 1 and 2, the dust emission correlates well with the dust extinction. On the other hand, figure 15b shows the τ_{353} map with the contours of N(H) of the L-component, from which we find that the dust emission correlates well with the L-component gas. N(H) of the L-component traces the dust emission in region 3. Those results strongly support that the L-component in region 3 is located behind the LMC.

Now that the dust clouds in regions 1 and 2 are likely located in front of almost all the stars, we can securely investigate the relation between the dust extinction and emission in those regions. In figure 16, we present the scatter plot of A_V and τ_{353} for each pixel of regions 1 and 2 with $\tau_{353} > 1.0 \times 10^{-5}$ for both regions. The figure shows that there is no systematic difference in the A_V-τ_{353} relation between regions 1 and 2. The black solid line is the result of the least-square fit to all the data points in regions 1 and 2, assuming that the relation between A_V and τ_{353} has a zero-point intercept. The estimated slope is $A_V/\tau_{353} = (1.86 \pm 0.04) \times 10^4$. Planck Collaboration (2014) gives $E(B-V)/\tau_{353} = 1.5 \times 10^4$ for the Galactic diffuse dust ($\tau_{353} < 5 \times 10^{-6}$). Assuming $R_V = 3.1$, we have $A_V/\tau_{353} = 4.6 \times 10^4$ for the Galactic diffuse dust, which is 2.4 times larger than our estimation of $A_V/\tau_{353} = (1.86 \pm 0.04) \times 10^4$ for the dust in regions 1 and 2 of the LMC H I ridge region. The same trend was reported for our Galaxy by Planck Collaboration (2014), who found that τ_{353}/N(H) systematically increases by a factor of ~ 2 from the diffuse to denser regions due to dust

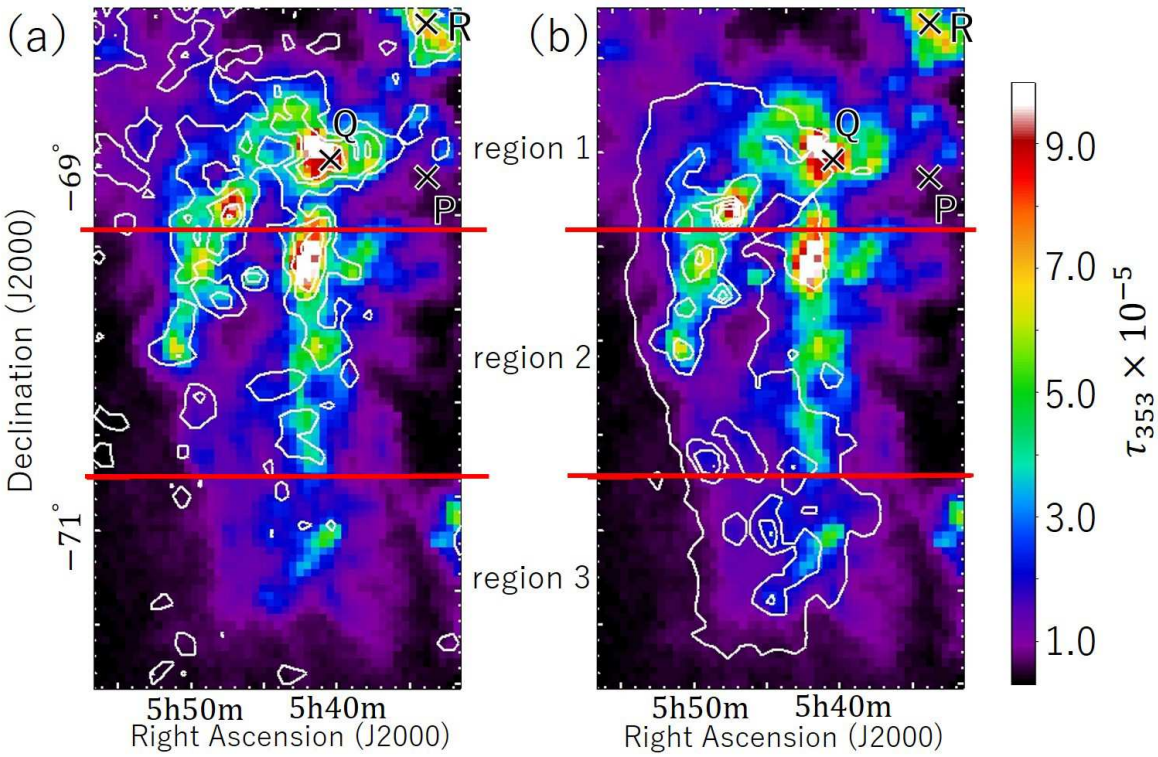


Fig. 15. Dust optical depth at 353 GHz, τ_{353} map superposed on the contours of (a) A_V(80%) detected with significance higher than 1σ and $A_V \geq$0.6 mag, and (b) N(H) of the L-component which are the same contours as in figure 12a. The contour levels in panel (a) are 0.6, 1.0, 1.3 and 1.7 mag. The red horizontal lines represent boundaries 1 and 2. The cross symbols are the same as those in figure 12.

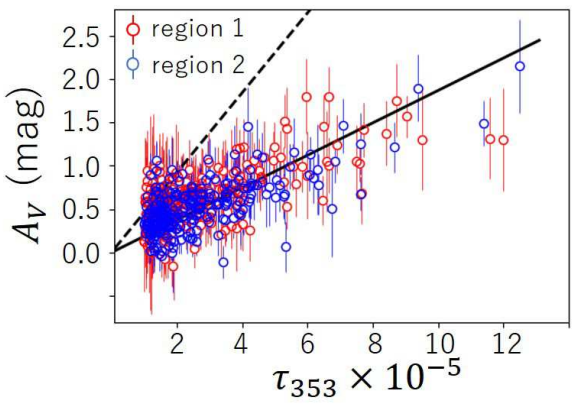


Fig. 16. Scatter plot between A_V and τ_{353} for regions 1 (red) and 2 (blue). Black solid line represents the result of the least-square fit to all the data points, while black dotted line represents the relation between A_V and τ_{353} for the diffuse Galactic dust.

aggregation to larger grains. Therefore, the relation between A_V and τ_{353} estimated in this paper is consistent with that in the dense ISM in our Galaxy, which suggests that the properties of large grains in the clouds of the I- and L-components are similar to those in our Galaxy.

6.3 Dust/gas ratio and CO-to-H_2 conversion factor

The A_V/N(H) values at $X = 40\%$ of the L-, I- and D-components are 1/10, 1/4 and 1/5, respectively, of the Galactic A_V/N(H) values of $\sim 5.3 \times 10^{-22}$ mag/(H cm^{-2}), while those at $X = 80\%$ are 1/5, 1/4 and 1/3 of the Galactic values, respectively. A_V/N(H) at $X = 40\%$ of all the components is consistent with that derived by Furuta et al. (2019) using the averaged dust extinction map (see table 1 and figure 13a in the present paper). On the other hand, A_V/N(H) at $X = 80\%$ of the L-component is 2 times higher than that derived by Furuta et al. (2019). This result can be interpreted as follows: since the L-component is penetrating the LMC disk (figure 14b), the averaged dust extinction of Furuta et al. (2019) would not trace all the dust in the L-component existing along the line of sight, which leads to under-estimation of the dust extinction. A_V/N(H) at $X = 80\%$ of the D-component is also 2 times higher than that derived by Furuta et al. (2019). This reasonably indicates that stars are randomly distributed between the foreground and background, and thus the averaged dust extinction would correspond to $\sim$1/2 of the total dust extinction.

Based on the scenario that the low metalliciy gas from

the SMC is accreted to and mixed in the H I ridge region (Fukui et al. 2017; Furuta et al. 2019), we compare the resultant $A_V/N(\mathrm{H})$ at $X = 80\%$ of each velocity component with the gas-to-dust ratios (GDRs) of the LMC and the SMC. Using Spitzer far-infrared, ACTA+Parkes H I 21 cm and NANTEN CO data, Bernard et al. (2008) and Leroy et al. (2007) obtained the averaged GDR about 3 times higher for the LMC and ∼10 times higher for the SMC, respectively, as compared to the Galactic GDR. Planck collaboration (2011) calculated the dust optical depth from the Planck data and suggested that the GDRs of the LMC and the SMC are 2.4 times and 13 times higher than the Galactic GDR, respectively. Roman-Duval et al. (2014) evaluated the GDRs in the Magellanic Clouds from dust and gas surface densities based on Herschel far-infrared, H I 21 cm, CO and Hα observations, and obtained the GDRs 3 times higher for the LMC and 6 times higher for the SMC than the Galactic value. In summary, the previous studies based on the dust emission indicate that the GDR is 2–3 times higher for the LMC and 6–13 times higher for the SMC than the Galactic value.

The $A_V/N(\mathrm{H})$ value at X=80% estimated for the D-component in the present study corresponds to ∼1/3 of the Galactic value (see figure 13a), which is consistent with the GDR of the LMC as mentioned above. This implies that our method works well to evaluate the dust extinction caused by the D-component gas. The $A_V/N(\mathrm{H})$ values estimated for the L- and I-components in the present study correspond to ∼1/5 of the Galactic value (figure 13a), which are intermediate values between the GDRs of the SMC and the LMC as mentioned above. Thus we suggest that the L- and I-component gases are mixed with the D-component gas due to the interaction between the LMC gas and the inflow gas from the SMC. Assuming that $A_V/N(\mathrm{H})$ of the inflow gas was originally 1/10 of the Galactic value, 1/5 of the Galactic $A_V/N(\mathrm{H})$ for the L- and I-components can be explained by a mixture of the inflow gas with the LMC gas having 1/3 of the Galactic $A_V/N(\mathrm{H})$ at a mass ratio of 1:1. This result is consistent with the mass fraction of the inflow gas (∼50%) in the H I ridge region expected from the ratio of τ_{353} to the H I intensity (Fukui et al. 2017).

As can be seen in figure 13b, the X_{CO} factors of each velocity component stay constant within the errors over the whole range of X% and are consistent with those in Furuta et al. (2019) (see table 1). This result indicates that the abundance ratio of CO to H_2 is relatively uniform within the clouds associated with each velocity component. The X_{CO} factors of the I- and D-components are similar to that of the LMC $\sim 2.9 \times 10^{20}$ cm^{-2}/(K km s^{-1}) obtained by Pineda et al. (2017), who correct the effect of the photodissociation of CO due to the lack of dust shielding. In addition, the X_{CO} factor of the L-component is in the range from that of the LMC $\sim 2.9 \times 10^{20}$ cm^{-2}/(K km s^{-1}) to that of the SMC $\sim 7.6 \times 10^{20}$ cm^{-2}/(K km s^{-1}) obtained by Pineda et al. (2017), which also supports the above picture of the inflow gas mixed with the LMC.

As a whole, the dust geometry and the difference in $A_V/N(\mathrm{H})$ and X_{CO} between the three velocity components suggest the galactic interaction between the LMC and the SMC in the H I ridge region. In our future work, we will apply this method to the entire LMC field to discuss a possibility of the overall massive star formation triggered by the galactic interaction.

7 Conclusion

We develop the method to evaluate A_V used in Furuta et al. (2019) by taking percentile values based on the X percentile method proposed by Dobashi et al. (2008). Using our new method, we construct the three-dimensional A_V map of the LMC H I ridge region. From comparison of A_V along the line of sight with $N(\mathrm{H})$ of different velocities, we decompose A_V into three velocity components, and evaluate the three-dimensional dust geometry and dust/gas ratios of the three velocities. Our main results are as follows:

1. The resultant dust geometry suggests that the L-component in the north region is penetrating the LMC disk, while that in the south region is located behind the LMC disk. In addition, the I-component (i.e., intermediate velocity) is located in front of almost all the stars in the LMC. This can be explained by the deceleration of the L-component through interaction with the D-component. These results indicate that the gas collision is on-going in the north prior to the south of the H I ridge region. Such a difference in the timing of the gas collision is consistent with the evolutionary sequence of molecular clouds in the H I ridge region found by Kawamura et al. (2009).
2. We compare the spatial distributions of the dust extinction $A_V(80\%)$ and the dust emission τ_{353} in the H I ridge region. We find that they are correlated well in the north while they are not in the south. The dust extinction is not detected whereas the dust emission exists and is well traced by $N(\mathrm{H})$ of the L-component in the south region. Those results strongly support the geometry that the L-component in the south region is located behind the LMC disk. The relation between A_V and τ_{353} suggests the dominance of large dust grains in the clouds of the I- and L-components, as found in dense clouds in our Galaxy.

3. $A_V(80\%)/N(\mathrm{H})$ of the D-component (Disk, see figure 14b) is $\sim$1/3 of the Galactic value, which is consistent with the gas-to-dust ratio (GDR) of the LMC estimated from the dust emission. On the other hand, $A_V(80\%)/N(\mathrm{H})$ of the L- and I-components is $\sim$1/5 of the Galactic value, which is an intermediate GDRs between the SMC and the LMC. This result suggests that the inflow gas from the SMC is mixed with the LMC gas at a mass ratio of 1:1 through the interaction between Magellanic Clouds in the H I ridge region. The difference in the X_{CO} factors of each velocity component suggests a result consistent with the above picture.

As a whole, our results support the scenario that massive star formation in 30 Dor has been triggered by the tidal interaction between the LMC and the SMC.

Acknowledgments

The IRSF project is a collaboration between Nagoya University and the SAAO supported by the Grants-in-Aid for Scientific Research on Priority Areas (A) (Nos. 10147207 and 10147214) and Optical & Near-Infrared Astronomy Inter-University Cooperation Program, from the Ministry of Education, Culture, Sports, Science and Technology (MEXT) of Japan and the National Research Foundation (NRF) of South Africa. This research was financially supported by Grant-in-Aid for JSPS Fellows Grant Number 20J12119.

References

Balbinot, E., et al. 2015, MNRAS, 449, 1129. doi:10.1093/mnras/stv356

Bekki, K. & Chiba, M. 2007a, PASA, 24, 21. doi:10.1071/AS06023

Bekki, K., & Chiba, M. 2007b, MNRAS, 381, L16

Bernard, J.-P., et al. 2008, AJ, 136, 919

Bessell, M. S., & Brett, J. M. 1988, PASP, 100, 1134

Bohlin R. C., Savage B. D., & Drake J. F., 1978, ApJ, 224, 132

Cardelli, J. A., Clayton, G. C., & Mathis, J. S. 1989, ApJ, 345, 245

Crowther, P. A., Schnurr, O., Hirschi, R., Yusof N., Parker R. J., Goodwin S. P., & Kassim H. A. 2010, MNRAS, 408, 731

Crowther, P. A., et al. 2016, MNRAS, 458, 624. doi:10.1093/mnras/stw273

De Marchi, G., & Panagia, N. 2014, MNRAS, 445, 93

Dickey, J. M., & Lockman, F. J. 1990, ARA&A, 28, 215

Dobashi, K., Bernard, J.-P., Hughes, A., Paradis, D., Reach, W. T., & Kawamura, A. 2008, A&A, 484, 205

Doran, E. I., Crowther, P. A., de Koter, A., et al. 2013, A&A, 558, A134

Elias, J. H., Frogel, J. A., & Humphreys, R. M. 1985, ApJS, 57, 91

Fukui, Y., et al. 1999, PASJ, 51, 745

Fukui, Y., et al. 2008, ApJS, 178, 56

Fukui Y., Torii K., Onishi T., Yamamoto H., Okamoto R., Hayakawa T., Tachihara K., & Sano H., 2015, ApJ, 798, 6

Fukui, Y., Tsuge, K., Sano, H., Bekki, K., Yozin, C., Tachihara, K., & Inoue, T. 2017, PASJ, 69, L5

Fukui Y., et al., 2019, ApJ, 886, 14

Furuta, T., Kaneda, H., Kokusho, T., Ishihara D., Nakajima Y., Fukui Y., & Tsuge K. 2019, PASJ, 71, 95

Indebetouw R., Wong T., Chen C.-H. R., Kepley A., Lebouteiller V., Madden S., & Oliveira J. M., 2020, ApJ, 888, 56

Imara, N., & Blitz, L. 2007, ApJ, 662, 969

Kato, D., et al. 2007, PASJ, 59, 615

Kaluzny J., Stanek K. Z., Krockenberger M., Sasselov D. D., Tonry J. L., & Mateo M. 1998, AJ, 115, 1016

Kawamura, A., et al. 2009, ApJS, 184, 1. doi:10.1088/0067-0049/184/1/1

Kim, S., Staveley-Smith, L., Dopita, M. A., Sault, R. J., Freeman, K. C., Lee, Y. & Chu, Y. 2003, ApJS, 148, 473

Lada, C. J., Lada, E. A., Clemens, D. P., & Bally, J. 1994, ApJ, 429, 694

Leroy A., Bolatto A., Stanimirovic S., Mizuno N., Israel F., & Bot C., 2007, ApJ, 658, 1027

Lombardi, M., & Alves, J. 2001, A&A, 377, 1023

Nakajima, Y., et al. 2005, AJ, 129, 776

Meixner, M., et al. 2006, AJ, 132, 2268

Pietrzyński, G., Graczyk, D., Gallenne, A., et al. 2019, Nature, 567, 200

Pineda, J. L., et al. 2017, ApJ, 839, 107

Planck Collaboration, 2011, A&A, 536, A17

Planck Collaboration, 2014, A&A, 571, A11

Roman-Duval, J., et al. 2014, ApJ, 797, 86

Schneider, F. R. N., et al. 2018, Science, 359, 69. doi:10.1126/science.aan0106

Tatton, B. L., et al. 2013, A&A, 554, A33

Tokuda K., et al., 2019, ApJ, 886, 15

Tsuge, K., et al. 2019, ApJ, 871, 44

Tsuge K., et al., 2021, ApJ, submitted (arXiv:2010.08816)

van der Marel, R. P., & Cioni, M.-R. L. 2001, AJ, 122, 1807

Westerlund, B. E. 1997, The Magellanic Clouds (New York: Cambridge Univ. Press), 243

Yao, X., et al. 2015, AJ, 150, 107

Yozin C., Bekki K., 2014, MNRAS, 443, 522. doi:10.1093/mnras/stu1132